

Comparison of quarter-wave retarders over finite spectral and angular bandwidths for infrared polarimetric-imaging applications

Samuel L. Wadsworth^{1,*} and Glenn D. Boreman^{1,2}

¹CREOL, The College of Optics and Photonics, University of Central Florida,
4000 Central Florida Boulevard, Orlando, Florida 32816, USA

²Department of Physics and Optical Science, University of North Carolina,
9201 University City Boulevard, Charlotte, North Carolina 28223, USA

*Corresponding author: samuel.l.wadsworth@saic.com

Received 7 July 2011; revised 24 August 2011; accepted 2 September 2011;
posted 7 September 2011 (Doc. ID 150662); published 20 December 2011

We compare three technological approaches for quarter-wave retarders within the context of polarimetric-imaging applications in the long-wave infrared (LWIR) spectrum. Performance of a commercial cadmium sulfide (CdS) crystalline waveplate, a multilayer meanderline structure, and a silicon (Si) form-birefringent retarder are evaluated under conditions of 8–12 μm broadband radiation emerging from an $F/1$ focusing objective. Metrics used for this comparison are the spectrally dependent axial ratio, retardance, and polarization-averaged power transmittance, which are averaged over the angular range of interest. These parameters correspond to the characteristics that would be observed at the focal-plane array (FPA) detector of an LWIR imaging polarimeter. © 2011 Optical Society of America

OCIS codes: 120.2130, 120.7000, 110.5405, 300.6340, 230.5440.

1. Introduction

Polarimetry is the process by which discrete states of polarization are resolved from an incident optical signal. This is most often performed with an arrangement of optical components, the combination and configuration of which enables decomposition of the detected radiation into polarization-resolved intensity coefficients, most commonly referred to as the Stokes parameters [1–4]. A typical polarimetry system consists of an analyzing linear polarizer (LP) and quarter-wave plate (QWP), which allow measurement of the four Stokes vector coefficients [2–4]. The QWP, in particular, is essential for measuring the circularly polarized (CP) component of the intensity, denoted as S_3 . Thermal infrared (IR) imaging polarimeters utilize this general approach over an operational spectral bandwidth that coincides with

the spectral responsivity of the imager's focal-plane array (FPA) detector. The irradiance falling on the FPA consists of a finite range of incident angles, which arrive from the focusing objective that allows for imaging of the intensity-based polarization field [5–7]. These conditions imply two requirements that QWPs must satisfy for optimum use in IR imaging polarimeters: the QWP must have broadband achromatic retardance, and it must do so over a range of incident angles consistent with the $F/$ of the imaging objective, since polarization components are typically placed in the converging beam directly in front of the FPA for direct integration with the pixelated sensor apparatus [6–8].

In order to determine which QWP technology is most suitable for IR polarimetric-imaging, we will compare polarimetric and power transmission metrics that would be discerned by the FPA detector. The FPA averages the received response over all angles and wavelengths, and thus we will do likewise for the characteristics of the QWP devices under

0003-6935/11/366682-07\$15.00/0
© 2011 Optical Society of America

investigation. We will introduce an entrance pupil area-averaged metric that accounts for the angular response of QWP components, which are assumed to be illuminated by a converging $F/1$ beam.

2. Selection of QWP Technologies for Testing in the LWIR

The QWP components selected for the current investigation represent an assortment of technologies that have been proposed for operation in the long-wave infrared (LWIR) band. They use materials that offer the best transmission throughput in this spectrum, as other material choices of birefringent QWP devices, such as crystalline silica, are inherently limited by the phonon-assisted attenuation that occurs beyond the mid-wave IR (MWIR) cutoff wavelength of $5\ \mu\text{m}$ [9,10]. We will therefore present a brief summary of the QWP technologies chosen for this study and the accompanying reasoning behind their selection.

The three QWPs investigated consist of a commercial crystalline cadmium sulfide (CdS) waveplate, a multilayer meanderline metamaterial, and a silicon (Si) form-birefringent retarder. They are shown in Fig. 1 with their respective TE and TM axes, which define the coordinate directions corresponding to the orthogonal birefringence axes of anisotropic material systems [2,3,10]. The CdS QWP component (Fig. 1(a)) was manufactured by II-VI Incorporated (model # 010201-7) for single-wavelength operation at $9.55\ \mu\text{m}$. Single-wavelength crystalline QWPs are typically composed of multiple orders of birefringent layers that collectively exhibit a large chromatic dispersion of the differential phase shift [11], and are thus not ideally suited for broadband IR polarimetry. The multilayer meanderline retarder (Fig. 1(b)) selected for this study represents a field of technology that has not yet been thoroughly investigated with regard to IR polarimetric-imaging. This device is the same 2-layer QWP component that was presented in [12], which is expected to exhibit achromatic polarimetric characteristics and angle-insensitive behavior, based upon past performance [12–15]. Multilayer meanderline QWPs have technological potential that could be employed in thermal IR po-

larimeters, especially considering that they can be fabricated into a compact planar form factor that facilitates integration with other polarization devices and pixelated IR sensors. The third QWP technology under consideration consists of an Si form-birefringent subwavelength grating (Fig. 1(c)). These have previously been investigated for use in thermal polarimetric-imaging [5–8], with desirable characteristics that enable ease of fabrication and integration with other FPA-coupled components [7,8,16–18]. Thus, the form-birefringent grating was evaluated with the other QWPs because it signifies the current pinnacle of state-of-the-art artificial birefringent materials that exhibit achromatic behaviors appropriate for broadband polarimetric-imaging. The Si form-birefringent retarder was modeled using finite-element method (FEM) electromagnetic software analysis [19] with a design that was scaled from reference [18], using conditions consistent with the measurement configurations and criteria for imaging with a focused $F/1$ beam.

3. Measurement and Computation of Area-Averaged Parameters

The polarimetric parameters of the CdS and meanderline QWPs were acquired by transmissive IR variable-angle spectroscopic ellipsometry (IR-VASE, from J. A. Woollam Corp.) over the 8–12 μm band. These parameters include δ , the differential phase shift, and ψ , the auxiliary angle, which determine the axial ratio (AR), defined as the ratio between the major and minor axes of the transmitted polarization ellipse [2,12,13]

$$AR = 1 / \left(\tan \left[\frac{1}{2} \arcsin \{ \sin(2 \cdot \psi) \cdot \sin(\delta) \} \right] \right). \quad (1)$$

Optimum QWP performance should yield 90° retardance for δ and a value of 1 for the AR [2,13]. In addition, the total power transmission was measured from the IR-VASE as a polarization-averaged quantity between incident s and p polarizations

$$T_{\text{total}} = \frac{1}{2} \cdot (T_s + T_p). \quad (2)$$

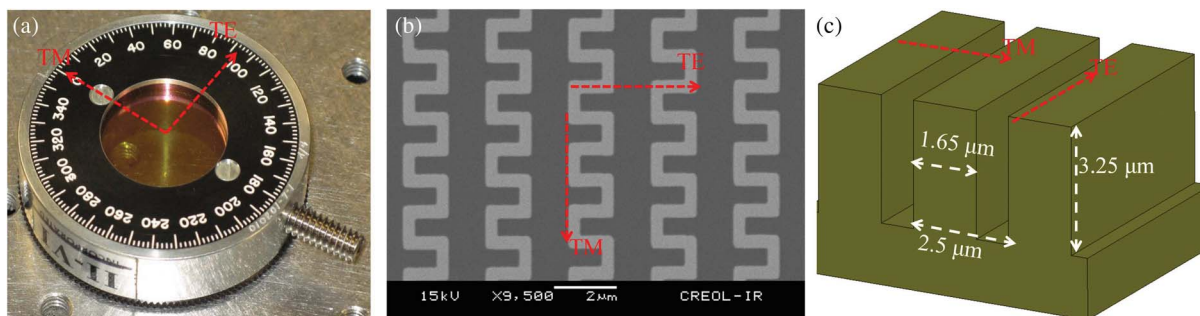


Fig. 1. (Color online) Three QWP approaches considered for the study, which consist of (a) crystalline CdS waveplate, (b) multilayer meanderline, and (c) Si form-birefringent subwavelength grating. Each component's respective TE and TM axes (in red) indicate the inherent anisotropy of the birefringent material systems. The simulated form-birefringent grating of (c) was modeled with high-resistivity Si in the LWIR spectrum, with its dimensions scaled from [18].

The measurement configuration on the IR-VASE apparatus allows for angular variation along one plane at a time, as shown in Fig. 2. Thus, for complete characterization, the device under test was rotated clockwise by 90° on the sample stage in order to evaluate the angular sensitivity along both planes of incidence that would be subjected to illumination from an $F/1$ system. The angle of incidence was varied in increments of 5.313°, from 0° to the maximum half-angle of an $F/1$ cone, which is 26.565°.

Although angle-dependent spectral polarimetric and power transmission quantities could be simply conveyed by listing the results from both the IR-VASE and numerical FEM procedures, it is our intention to replicate the equivalent angle-averaged metrics that would be observed at the plane of the FPA sensor. As Fig. 3 demonstrates, the FPA is illuminated by a discrete angular spectrum of focused radiation that arrives from an $F/1$ imaging optic. Therefore, because the FPA pixels are not inherently sensitive to angular stimuli, the collected irradiance would be perceived as a single optical signal, whose response is averaged over the incident cone of illumination. An equivalent picture of this situation can be composed by equating each incident light ray in the $F/1$ cone to an approximate area of the $F/1$ objective, from which that particular ray emerged after refracting through the $F/1$ lens system. This is shown in Fig. 3, where a specified angle of incidence θ_s within the impinging $F/1$ cone directly correlates to a discrete area on the effective aperture of an $F/1$ objective (assumed to be circular for convenience). Thus, instead of averaging over a discrete summation of angles, one can average the aggregated response that emerges from each discretized area that encompasses the entire circular pupil zone of the $F/1$ objective. This essentially accounts for the same



Fig. 2. (Color online) Details of the IR-VASE system with axis of rotation (in white) and plane of incidence with surface normal (in red) indicated.

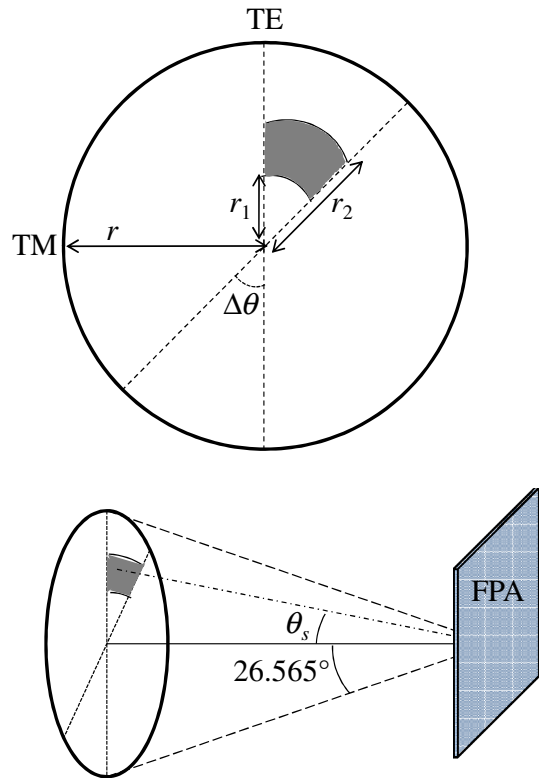


Fig. 3. (Color online) Depiction of entrance pupil aperture with a finite wedge area representing the average axial response from an angle of incidence within a full $F/1$ cone.

angle-averaged response that would be received at the FPA, and the discretized areas provide an effective weighting factor for each ray that exits the $F/1$ objective, assuming that the aperture is uniformly illuminated. The ensuing area-averaged polarimetric and power transmission metrics (either directly measured or numerically simulated in the case of the Si form-birefringent QWP) can then be quantified over the entire entrance pupil of the focusing $F/1$ objective by employing a discrete summation over the angular response of each QWP component

$$P = \sum_{\theta_i, \theta_s} \frac{(1/2) \cdot \Delta\theta \cdot ((r_2(\theta_s))^2 - (r_1(\theta_s))^2)}{\pi \cdot r^2} \cdot \dots \cdot (P_{TE}(\theta_s) \cdot \cos^2(\theta_i) + P_{TM}(\theta_s) \cdot \sin^2(\theta_i)), \quad (3)$$

where P_{TE} and P_{TM} are the parameters obtained from the separate scans over the TE and TM axes of the material, θ_s represents the angle of incidence, θ_i is the angle of rotation around the perimeter of the entrance pupil aperture, and $\Delta\theta$ is indicative of the finite wedge area in the plane of the entrance pupil, as shown in Fig. 3. The radii r_2 and r_1 are the outer and inner radii of the wedge, and r is the unit radius of the entire aperture. This formulation assumes that the angular scans along the associated TE and TM axes account for the variation required to portray a full $F/1$ cone of focused illumination, since each material has a symmetric response about a common

axis. The reasoning behind this computation is, as suggested by Fig. 3, that each incident angle of the scans that cover the TE and TM axes has an associated finite area given by a wedge with a discrete wedge angle $\Delta\theta$ and inner and outer radii that define the boundaries of that wedge. Each wedge therefore has a weighted contribution to the emerging $F/1$ beam that is proportional to the fractional area of the pupil zone through which light propagates, and it is given by

$$A_{\text{wedge}} = (1/2) \cdot \Delta\theta \cdot ((r_2(\theta_s))^2 - (r_1(\theta_s))^2) \quad (4)$$

for a specified angle of incidence θ_s . The entire response over the entrance pupil is therefore given by the summation of the averaged parameter response over each wedge in the plane of the aperture, the averaging taking into account the separate axial responses from the TE and TM scans, as shown in the second part of Eq. (3). This summation is subsequently divided by the area of the circular aperture.

Ideally, the wedge angle $\Delta\theta$ is chosen such that θ_i can be split up into equal fractions of $2 \cdot \pi$. Thus, when Eq. (3) is summed over all corresponding angles, the total pupil-averaged polarimetric and transmittance metrics amount to the equivalent angle-averaged characteristics that would be observed by the FPA from a full $F/1$ cone. Note that, for the above calculations, θ_i was swept from 0 to $2 \cdot \pi$ radians in increments of $2 \cdot \pi/10$ radians (thus, $\Delta\theta = 2 \cdot \pi/10$), and θ_s was swept from 0 to $26.565 \cdot \pi/180$ radians in increments of $5.313 \cdot \pi/180$ radians. The area-based weighting of the incident angles, which comprise the emerging $F/1$ beam, was subsequently implemented by associating each θ_s with discrete values of r_1 and r_2 , the inner and outer radii of the wedge areas that constitute the circular aperture of the entrance pupil. These radii are shown below in Table 1 for each θ_s up to the half-angle of the impinging $F/1$ cone. Additionally, the area-averaged parameter P in Eq. (3) can be used to represent any of the following quantities: the phase shift δ , the axial ratio AR, or the polarization-averaged transmittance T_{total} of Eq. (2).

4. Results and Related Discussion

A. Polarimetric Data

The first evaluation of the QWPs considered in this study centers around the wavelength dependence of

Table 1. Values of Wedge Radii r_1 and r_2 with Respect to the Incident Angle θ_s (Normalized by Unit Radius r)

θ_s	r_1	r_2
0°	0	0.094
5.313°	0.094	0.282
10.626°	0.282	0.476
15.939°	0.476	0.678
21.252°	0.678	0.894
26.565°	0.894	1

the retrieved area-averaged polarimetric quantities, in order to gauge which component portrays the desired achromatic behavior. These quantities consist of δ , the differential phase shift, and AR, the axial ratio. As shown in Fig. 4, the phase shift resulting from the form-birefringent and multilayer meanderline QWPs is highly achromatic and close to the desired value of 90°. Their AR values are also below 2 throughout the majority of the LWIR spectrum, which is a good indication of a high percentage of radiation converted into CP [20]. As expected, it is seen that the crystalline CdS QWP suffers from significant chromatic-dispersion effects, and thus cannot be considered as a viable solution for broadband LWIR imaging polarimeters. Furthermore, crystalline retarders are typically expensive and bulky in size, and are not easily integrated with

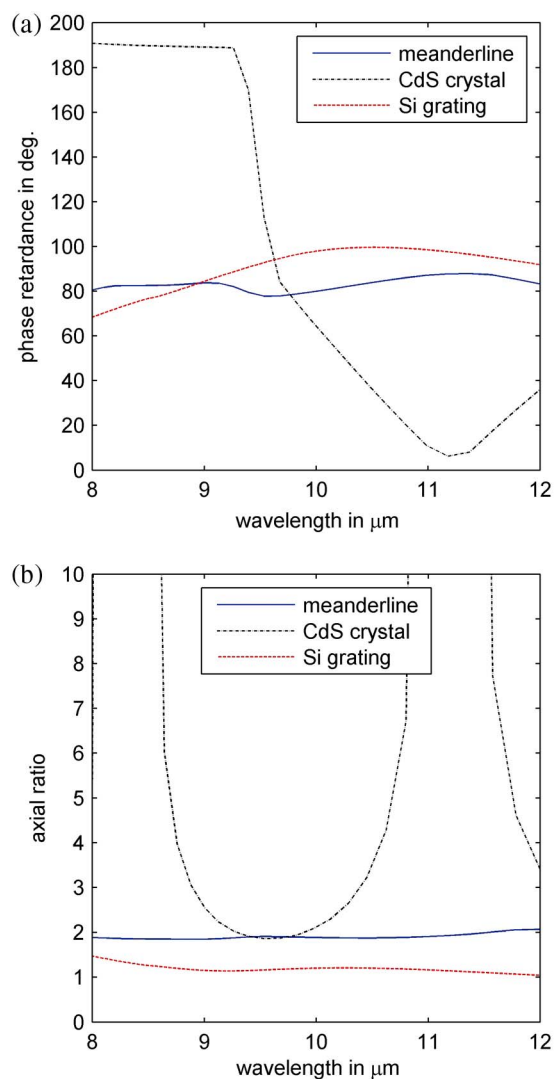


Fig. 4. (Color online) Area-averaged polarimetric results for (a) the phase retardance and (b) the axial ratio of the QWP devices in the current study. The data for the CdS and meanderline QWPs were acquired by IR-VASE measurements, whereas the Si form-birefringent grating was simulated using numerical FEM analysis.

an FPA sensor or with other low-profile polarization components.

In spite of the idealized polarimetric behavior exhibited by the meanderline and Si grating QWPs, there are some observable anomalies on Fig. 4 that contribute to the degradation of the angle-averaged performance of said wave retarders. Specifically, the meanderline retarder, although eliciting a high-percentage conversion of LP into CP, actually produces more of an elliptic beam upon propagation through the multilayered structure. This is apparent when its axial ratio is compared to that of the Si form-birefringent grating, which takes on an averaged value of approximately 1.2 throughout the LWIR. The increase in beam ellipticity is particularly due to the disparity between the surface impedance discontinuities of the TE and TM modes of the meanderline structure, which is intrinsically anisotropic due to the geometrical configuration of the metallic scatterers (see Fig. 1(b)) [12–15]. Secondly, the phase shift of the meanderline QWP exhibits two noticeable dips in its spectrum that signify further departure from ideal behavior. These spectral minima correspond to the phonon modes of benzocyclobutene (BCB), the dielectric layer that was used in the construction of the multilayer component [21]. However, as shown in Fig. 5, this behavior can be corrected by substituting for a low-loss dielectric film, such as yttrium fluoride (YF_3) [22]. The inclusion of YF_3 was simulated in the FEM analysis software, since deposition of YF_3 dielectric films often contaminates evaporation chambers with harmful fluoride-based compounds that can potentially ruin other processes. Nonetheless, the simulated structure with YF_3 allows for a much smoother response over the wavelength band of interest, such that the polarimetric qualities become equal to those provided by the form-birefringent QWP device, which are also plotted on Fig. 5. Therefore, the polarization characteristics of multilayer meanderline QWPs can match the proposed specifications of thermal imaging polarimeters, and can furthermore provide improved quality over the previous response of multilayer meanderlines when YF_3 is considered for the dielectric layer, thereby permitting the structure to veritably compete with state-of-the-art Si form-birefringent technology.

B. Power Transmission and Wavelength-Averaged Data

The percentage power transmission for a given QWP structure must also be evaluated, since a higher throughput increases the signal-to-noise ratio (SNR) and hence the accuracy of intensity-based polarization detection, with a corresponding decrease in residual error. Therefore, as shown in Fig. 6, the area-averaged transmission was determined for all three structures under investigation, with the CdS crystalline QWP being the best. This is due to a number of factors, the first of which comes from the dual-sided antireflection coatings applied to each facet of the CdS components depicted in Fig. 1. The second

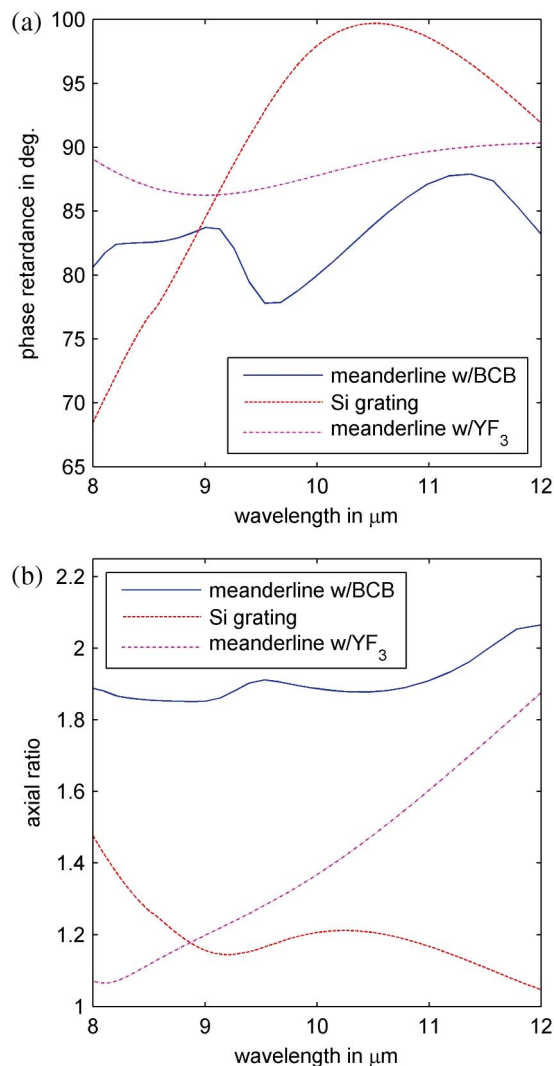


Fig. 5. (Color online) Area-averaged polarimetric data consisting of (a) phase retardance and (b) axial ratio. Results are plotted and compared for the measured 2-layer meanderline QWP that has BCB dielectric incorporated into its structure, and the simulated 2-layer meanderline device with low-loss YF_3 film. The data from the Si form-birefringent grating is also shown for comparison purposes.

factor is due to the material choices that allow for the Si form-birefringent and multilayer meanderline QWPs to arrive at nearly the same percentage in transmission levels. Although broadband antireflection (BBAR) coatings are commonplace in practice, examples of fabricated form-birefringent grating retarders in the literature typically measure the polarimetric and transmission qualities without applying such BBAR layers that would otherwise enable noticeable increases in power throughput [16–18]. For this reason, the Si form-birefringent retarder was initially simulated with the back side of the Si substrate un-coated, as to reflect the typical measurement condition found in the literature. Additionally, the layer of BCB in the multilayer meanderline QWP limits the amount of measured transmission via substantial attenuation of the optical signal,

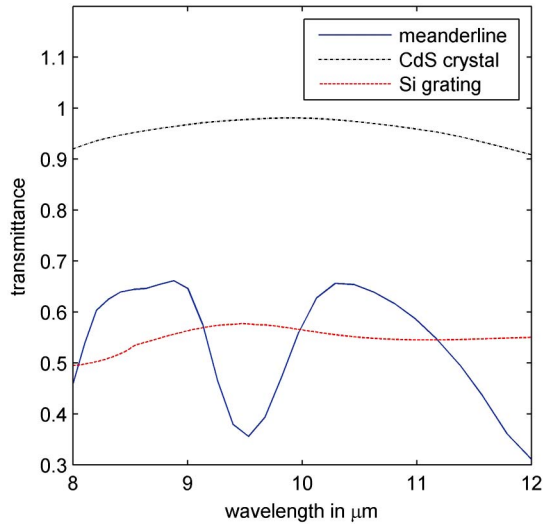


Fig. 6. (Color online) Area and polarization-averaged power transmission, where the CdS and meanderline QWPs are measured by IR-VASE, and the Si grating is simulated using the numerical FEM approach.

especially near the 9.5 and 12 μm phonon-mode resonances [21]. Thus, it is desirable to investigate ways to improve the transmission performance, especially since both the multilayer meanderline and form-birefringent retarders exhibit nearly achromatic behavior with regard to the observed differential phase shift and axial ratio at the plane of the FPA.

We will now present numerical results from simulations that alter the material compositions of the form-birefringent and multilayer meanderline QWPs, hopefully resulting in improved transmission performance. As before, we substitute the BCB dielectric layer with YF_3 for the meanderline metamaterial QWP device, and assume that the back side of the Si form-birefringent grating is coated with a multilayered BBAR dielectric structure. Accounting for these changes yields the power transmittance quantities shown in Fig. 7.

Referring to Fig. 7, we can observe a distinct difference between the form-birefringent and meanderline QWP technologies. The limiting factor that was hindering the form-birefringent structure, the Fresnel loss at the uncoated back side of the Si substrate, is now removed with the assistance of a BBAR coating [12,23]. Thus, the only scattering losses are those at the initial grating interface, which is highly transmissive because of its own antireflection-like effective medium properties [7,16–18]. Therefore, even though the meanderline QWP utilizes low refractive-index materials, such as barium fluoride (BaF_2) substrates and YF_3 dielectric layers, the losses of the metallic meanderline inclusions cannot be easily circumvented even with optimized thicknesses of YF_3 interlayer films [24]. The most feasible path forward for improvement of meanderline devices is to increase the number of layers in the meanderline, which would subsequently reduce the effective linewidths of the metallic meanderline con-

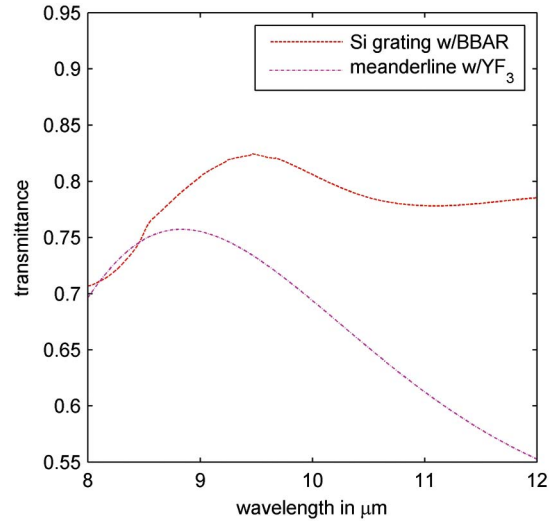


Fig. 7. (Color online) Area and polarization-averaged power transmission of a BBAR-coated Si form-birefringent grating and a meanderline QWP with YF_3 as the dielectric layer. Both structures were simulated with FEM analysis.

ducting elements and increase the percentage of transmission throughput [12]. However, validation of this approach would require additional analysis and experimentation, since an optimized 3-layer (or more) meanderline device has not yet been experimentally proven to provide suitable transmission improvements. For the present study, the performance of the 2-layer meanderline retarder is used for comparison purposes, especially since its spectral polarimetric quantities exhibit ideal behavior that can be contrasted with those from the Si form-birefringent grating. With all the appropriate data taken into consideration, the polarimetric performance of the two idealized structures is more or less equal, with some slight improvement in the phase retardance uniformity of the meanderline QWP with YF_3 , which subsequently reduces the error in the detected CP-based irradiance signal. The form-birefringent retarder, on the other hand, exceeds the power transmission of the meanderline QWP by an average of about 11% over the LWIR, so it still retains an advantage in terms of throughput, although there is some finite portion of stray light that emanates from the ± 1 orders of the TM-associated grating modes. However, the accumulated entrance pupil area-averaged percentage of incident irradiance that proliferates through these diffraction orders is less than 2%, which would most likely be dispersed among the background signal of the FPA,

Table 2. Summary of Wavelength and Area-Averaged Data

	δ	AR	T_{total}
Meanderline with BCB	$82.8^\circ \pm 2.8^\circ$	1.89 ± 0.06	0.54 ± 0.11
CdS crystal	$113^\circ \pm 77.5^\circ$	15 ± 23	0.96 ± 0.02
Si grating (bare)	$88.9^\circ \pm 9.9^\circ$	1.21 ± 0.09	0.55 ± 0.02
Si grating (with BBAR)	$88.9^\circ \pm 9.9^\circ$	1.21 ± 0.09	0.78 ± 0.03
Meanderline with YF_3	$88^\circ \pm 1.4^\circ$	1.35 ± 0.23	0.67 ± 0.06

so this would have a negligible effect upon polarization image quality. The comparison of the three technologies investigated can be summarized in terms of wavelength-averaged metrics, which are seen in Table 2 below.

5. Conclusion

Comparison of three QWP technologies in the LWIR spectrum was carried out with particular emphasis on applications relating to IR polarimetric-imaging. Therefore, the polarimetric and transmission metrics were averaged over the angular and wavelength response that would be observed at the FPA. This was done by computing the entrance pupil area-averaged parameters that would result from illumination by an $F/1$ focusing objective. The resulting metrics indicate that both the form-birefringent and the multilayer meanderline QWPs perform satisfactorily to satisfy requirements for broadband imaging, although the meanderline devices have a slight advantage in terms of the uniformity of phase retardance over the LWIR spectrum. This ultimately leads to a reduction of polarization-associated errors at the FPA. However, it was also demonstrated that Si form-birefringent retarders have an advantage regarding power transmission throughput when BBAR coatings are applied to the back side of the substrate. Nonetheless, it is possible that future meanderline devices with additional layers could achieve this transmission performance with further optimization of the dielectric-layer thicknesses and structural linewidths and geometries. Thus, multilayered metamaterials represent a viable new technology for angle-insensitive achromatic QWPs in the LWIR spectrum, which should be evaluated along with form-birefringent retarders for potential use in broadband imaging polarimetric applications.

References

1. T. Carrozi, R. Karlsson, and J. Bergman, "Parameters characterizing electromagnetic wave polarization," *Phys. Rev. E* **61**, 2024–2028 (2000).
2. D. Goldstein, *Polarized Light*, 2nd ed. (Marcel Dekker, 2003).
3. R. M. A. Azzam and N. M. Bashara, *Ellipsometry and Polarized Light* (Elsevier, 1977).
4. L. Mandel and E. Wolf, *Optical Coherence and Quantum Optics*, (Cambridge University, 1995).
5. H. Kikuta, K. Numata, M. Muto, K. Iwata, H. Toyota, K. Moriwaki, T. Yotuya, and H. Sato, "Polarization imaging camera with form birefringent micro-retarder array," in *Frontiers in Optics*, Technical Digest (CD) (Optical Society of America, 2003), paper ThRR3.
6. C. S. L. Chun, "Microscale waveplates for polarimetric infrared imaging," *Proc. SPIE* **5074**, 286–297 (2003).
7. S. A. Kemme, A. A. Cruz-Cabrera, R. R. Boye, T. Carter, S. Samora, C. Alford, J. R. Wendt, G. A. Vawter, and J. L. Smith, "Micropolarizing device for long wavelength infrared polarization imaging," Sandia Report SAND2006-6889 (Sandia National Laboratories, 2006).
8. R. B. Boye, S. A. Kemme, J. R. Wendt, A. A. Cruz-Cabrera, G. A. Vawter, C. R. Alford, T. R. Carter, and S. Samora, "Fabrication and measurement of wideband achromatic waveplates for the mid-infrared region using subwavelength features," *J. Microlith. Microfab. Microsyst.* **5**, 043007 (2006).
9. E. L. Geiszelmann, S. F. Jacobs, and H. E. Morrow, "Simple quartz birefringent quarter-wave plate for use at $3.39\ \mu\text{m}$," *J. Opt. Soc. Am.* **59**, 1381–1383 (1969).
10. M. Fox, *Optical Properties of Solids* (Oxford University, 2001).
11. P. D. Hale and G. W. Gay, "Stability of birefringent linear retarders," *Appl. Opt.* **27**, 5146–5153 (1988).
12. S. L. Wadsworth and G. D. Boreman, "Analysis of throughput for multilayer infrared meanderline waveplates," *Opt. Express* **18**, 13345–13360 (2010).
13. S. L. Wadsworth and G. D. Boreman, "Broadband infrared meanderline reflective quarter-wave plate," *Opt. Express* **19**, 10604–10612 (2011).
14. J. S. Tharp, J. Alda, and G. D. Boreman, "Off-axis behavior of an infrared meander-line waveplate," *Opt. Lett.* **32**, 2852–2854 (2007).
15. J. S. Tharp, B. A. Lail, B. A. Munk, and G. D. Boreman, "Design and demonstration of an infrared meanderline phase retarder," *IEEE Trans. Antennas Propag.* **55**, 2983–2988 (2007).
16. D. L. Brundrett, E. N. Glytsis, and T. K. Gaylord, "Subwavelength transmission grating retarders for use at $10.6\ \mu\text{m}$," *Appl. Opt.* **35**, 6195–6202 (1996).
17. F. Xu, R.-C. Tyan, P.-C. Sun, Y. Fainman, C.-C. Cheng, and A. Scherer, "Fabrication, modeling, and characterization of form-birefringent nanostructures," *Opt. Lett.* **20**, 2457–2459 (1995).
18. G. P. Nordin and P. C. Deguzman, "Broadband form birefringent quarter-wave plate for the mid-infrared wavelength region," *Opt. Express* **5**, 163–168 (1999).
19. R. T. Remski, "Analysis of photonic bandgap surfaces using Ansoft HFSS," *Microwave Journal* **43**, 51–68 (2000).
20. J.-C. Zhang, Y.-Z. Yin, and J.-P. Ma, "Multifunctional meander line polarizer," *Prog. Elect. Research Lett.* **6**, 55–60 (2009).
21. W. R. Folks, J. C. Ginn, D. J. Shelton, J. S. Tharp, and G. D. Boreman, "Spectroscopic ellipsometry of materials for infrared micro-device fabrication," *Phys. Status Solidi C* **5**, 1113–1116 (2008).
22. D. F. Bezuidenhout, K. D. Clarke, and R. Pretorius, "The optical properties of YF_3 films," *Thin Solid Films* **155**, 17–30 (1987).
23. H. A. Macleod, *Thin-Film Optical Filters* (Elsevier, 1969).
24. J. E. Reynolds, B. A. Munk, J. B. Pryor, and R. J. Marhefka, "Ohmic loss in frequency-selective surfaces," *J. Appl. Phys.* **93**, 5346–5358 (2003).